ACS OMEGA

Open Access

http://pubs.acs.org/journal/acsodf

Article

Geometric and Electronic Effects in the Binding Affinity of Imidazole-Based N-Heterocyclic Carbenes to Cu(100)- and Ag(100)-Based Pd and Pt Single-Atom Alloy Surfaces

Matthew D. Hanson* and Scott M. Simpson*

Cite This: *ACS Omega* 2023, 8, 37402−37412

Read Online

ACCESS | Metrics & More | Article Recommendations | Supporting Information

ABSTRACT: We have conducted nonlocal periodic density functional theory (DFT) calculations of N-heterocyclic carbenes (NHCs) adsorbed to Pd/Cu(100), Pt/Cu(100), Pd/Ag(100), and Pt/Ag(100) single atom alloys (SAAs) utilizing the nonlocal optPBE-vdW functional. NHCs with electron donating groups (EDGs) are predicted to bind more strongly to the SAA surface compared to NHCs functionalized with electron withdrawing groups (EWGs). Our calculations show that NHCs typically bind to SAA geometries containing a small space between the heteroatom sites for the SAAs considered. Generally, this pattern is predicted to persist for a single NHCs or for a pair of NHCs bound to the SAA surfaces. Approximate linear relationships between NMR-based parameters and NHC-SAA binding energies are uncovered. We predict that the binding of NHCs to SAA surfaces is composition-dependent and heteroatom geometry dependent.

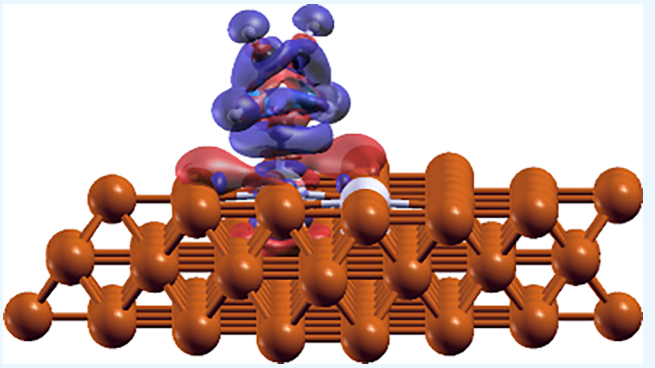

INTRODUCTION

A combination of increasing risks of fossil-fuel scarcity, geopolitical tensions stemming therefrom, and environmental degradation from fossil fuel extraction and anthropogenic climate change has spurred an increased interest in alternative energy sources. While wind, solar, and nuclear electrical energy are promising for various applications, there has also been increased interest in the use of carbon-neutral combustion fuels such as hydrogen gas. Hydrogen has a significant gravimetric energy density that outperforms that of traditional fuels such as gasoline due to the highly exothermic combustion reaction between hydrogen and oxygen gases to form water as a byproduct.[1,2] Hydrogen gas thus serves as a prototypical alternative combustion fuel. Unfortunately, the strongly exothermic behavior of this reaction also makes hydrogen fuel intrinsically problematic, as there is a high risk of catastrophic containment failure stemming from mechanical stress: for example, a vehicular crash or puncture of a storage vessel. While this risk is relatively small for immobile hydrogen fuel cells, it must be addressed for hydrogen to be a viable fuel in mobile and household applications. Concern about this risk comes with historical precedent, with incidents such as the Hindenburg and Challenger disasters proving particularly noteworthy. Safe storage of hydrogen gas therefore must address the containment of a large amount of fuel under nearly ambient conditions while also mitigating risk of explosive failure.[2]

One potential avenue toward solving this problem relies upon the molecular corking effect discovered and characterized by the Sykes group.[3−5] This effect is based on the interaction of hydrogen gas with bulk metal surfaces. It is well-known that hydrogen will separate into individual H atoms on pure metallic surfaces such as Pd or Pt and at heteroatom sites on single-atom alloy (SAA) surfaces.[6−19] The former effect has been used in catalytic hydrogenation chemistry for well over a century. The dissociated H atoms can then diffuse across the metal surface while remaining adsorbed, even if the metal surface is primarily composed of coinage metals such as Cu or Ag. Once the H−H bond is cleaved, the hydrogen atoms become more chemically inert, thus making adsorption of hydrogen to metal surfaces (or even nanoparticles) an attractive storage option.[3−5,20,21] Because the H atoms can diffuse across the surface relatively easily, a large amount of atomistic hydrogen can be theoretically stored on SAAs.[1,22] Unfortunately, the H atoms can relatively easily recombine at the heteroatom sites and leave as reactive H_2. This makes

Received: July 24, 2023
Accepted: September 12, 2023
Published: September 27, 2023

https://doi.org/10.1021/acsomega.3c05376
ACS Omega 2023, 8, 37402−37412

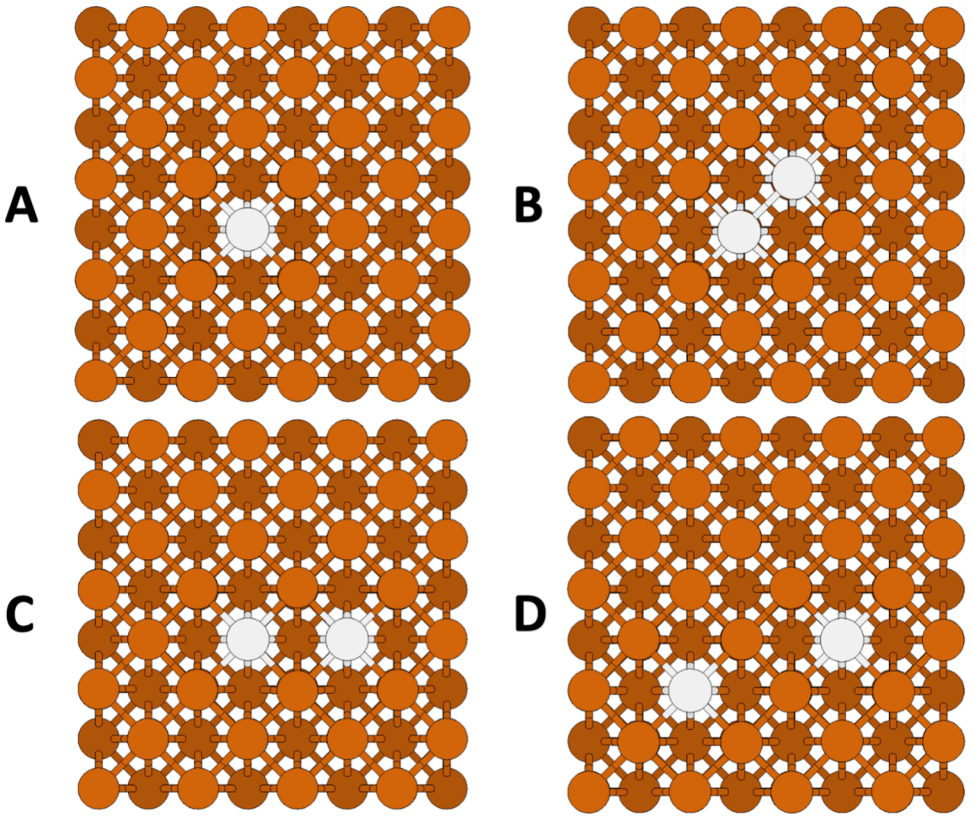

Figure 1. Top-down cartoon representation of the (A) s_0, (B) s_1, (C) s_2, and (D) s_3 geometries of the Pd/Cu(100) SAA surfaces. Lower depth of the atoms in the surface is indicated by darker color shading. Copper/palladium atoms are represented with orange/white spheres, respectively.

controlling the heteroatom sites critical to the storage and release of the hydrogen gas as fuel.[3−5,23]

The molecular corking effect exploits the importance of the heteroatom sites by utilizing a ligand, such as carbon monoxide, that "corks" the heteroatom sites through preferential binding. Sykes et al. have shown through temperature-programmed desorption (TPD) experiments that the desorption of the corking ligand thermodynamically controls the release of reactive hydrogen gas from the surface.[3−5,9,13,21,24] Unfortunately, the carbonyl ligand studied by the Sykes group only raised the desorption temperature from around 210 to roughly 260 K for a Pd/Cu(111) (heteroatom/metal with Miller indices) SAA and from 230 to 280 K for a Pt/Cu(111) SAA. Due to the low-temperature desorption of carbon monoxide, stronger-binding ligands that can serve as molecular corks on SAAs need to be investigated. It is also desirable that these ligands have highly tunable electronic properties, so that engineering applications are not strictly limited to a particular temperature regime.

Molecular corks can also affect the structure and reactivity of catalytic metal surfaces.[6−8,10,11,25−33] Recently, the use of CO on Pd/Au(111) SAAs to modify the active sites of SAA catalysts has been demonstrated via density function theory (DFT) calculations and then confirmed via experiment.[34] DFT studies have shown the ability of CO to influence the morphology of 15 distinct SAAs.[34] This shows that adsorbates can induce changes in surfaces that directly impact catalytically active sites, which can result in an improvement or degradation in the activity for SAA catalysts. For example, aggregated Pd sites on Au are required for O_2 activation in the CO oxidation reactions, whereas single Pd sites are inactive for the reaction.[35] Another example is the methane oxidation reaction, which requires Pd nanoparticles to function. Decomposition of the nanoparticles into single Pd atoms leads to a steep drop in reactivity.[36] A further example includes the complete hydrogenation of ethylene to ethane. This reaction does not take place on dispersed Ni/Cu and Pt/Cu SAAs and requires clusters of Ni and Pt.

Recently, N-heterocyclic carbenes (NHCs) have been suggested as potentially viable molecular corks for hydrogen storage under ambient conditions due to their strong σ-donor and π-back-bonding capability.[4,37−42] The electronic properties of NHCs can also be easily tuned by modification of the substituents around the ring. Extensive experimental and theoretical characterization of the properties of these carbenes exist in the literature.[37,43−47] Further, we have recently demonstrated that imidazole-based NHCs have a strong and tunable binding affinity to SAAs on the basis of the electronic properties of the ring substituents. In that study, a connection was established between the calculated NMR shielding constant for the Se atom in a gas-phase NHC-selenourea adduct, which is intimately related to the electronic properties of the substituents, and the binding energy of the NHC to an SAA surface.[4] It was determined that NHCs substituted with electron-donating groups (EDGs) had stronger binding affinities, while NHCs substituted with electron-withdrawing groups (EWGs) had weaker binding affinities to the SAAs. This is significant because an independent parameter estimating the electronic character of the substituents is closely related to the binding affinity of NHCs to a surface in a completely different system. In this article, we will expand on this work and demonstrate that SAA heteroatom geometry and the substituents of the NHCs bound to neighboring sites have

https://doi.org/10.1021/acsomega.3c05376
ACS Omega 2023, 8, 37402−37412

important implications for the binding affinity of the NHCs to the surfaces.

COMPUTATIONAL DETAILS

Periodic simulations of the NHCs and the SAA surfaces were performed by using the VASP 5.3.3 software package. The optPBE-vdW functional was used to account for nonlocal dispersion interactions, and the projector-augmented wave (PAW) method was used to treat core states along with a planewave energetic cutoff of 500 eV.[48−53] The Γ-centered Monkhorst−Pack scheme was used to generate 3 × 3 × 1 k-point meshes for the calculations, which are sufficient due to the relatively large periodic simulation box.[54] The H 1s electrons, C, N, O, and F 2s and 2p electrons, Cl 3s and 3p electrons, Cu 4s and 3d electrons, Pd 5s and 4d electrons, and Pt 6s and 5d electrons were treated explicitly. A dipole correction along the z-axis was also employed by using the IDIPOL tag in VASP.

The SAA surface slabs were created by first optimizing the coordinates and lattice parameters for the minimal cubic unit cell of the Cu or Ag bulk metal starting from the libraries in the program Avogadro.[55] The lattice parameters for the bulk metals were optimized with a 31 × 31 × 31 k-point mesh to ensure convergence. This was followed by cutting the lattice to make a three-layer surface with (100) Miller indices and 32 atoms in each layer (96 total atoms) using Avogadro. Individual metal atoms on the surface were replaced with Pd or Pt heteroatoms, and the top layer of the surface was permitted to relax with the lattice vectors fixed. This resulted in orthorhombic unit cells with dimensions along the *x*, *y*, and *z* axes of 14.60 Å × 14.60 Å × 20 Å for Cu-based SSAs and 16.65 Å × 16.65 Å × 20 Å for Ag-based SAAs. The 20 Å vector along the *z*-axis was selected to ensure that the surfaces and NHCs bound to them would not have spurious interactions orthogonal to the surface in periodic calculations. One surface heteroatom geometry was generated for each metal combination with only a single Pd or Pt heteroatom in the top layer, which we label s_0. Three different SAA geometries with matching pairs of heteroatoms spaced one, two, or three surface sites apart, labeled s_1, s_2, and s_3, respectively, were generated for each metal combination. When we refer to surface geometry in this work, we are exclusively referring to the arrangement of the heteroatoms. The lower two layers of the surface were fixed to dramatically speed up optimizations. The s_0, s_1, s_2, and s_3 geometries of the Pd/Cu(100) SAA are illustrated as cartoons using the XCrysDen modeling software in Figure 1.[56]

Gas-phase NHC molecular geometries were determined by optimizing individual NHC molecules in a cell with dimensions identical to those used in the corresponding SAA surface simulations. Before optimizing the NHC adsorbed to the SAA surface, the NHC coordinates were rotated so that the carbene C was oriented toward the surface of the SAA and shifted so that the carbene C was 2 A° above the heteroatom. The resulting geometries have the NHC plane perpendicular to the metal surface.[37−40,57−60] When the optimization of the NHCs on SAAs was performed, all atoms of the NHC molecules were allowed to relax along with the top layer of the SAA surface.

For pairs of NHCs on SAAs, the optimized NHC coordinates were once again reoriented so that the carbene C on each NHC pointed toward the SAA surface directly above one of the heteroatoms, as shown in Figure 2. For pairs of NHCs, the NHC molecules were then rotated such that the normal vectors to the plane of the NHC ring aligned with the heteroatom-heteroatom vector. Finally, the NHC coordinates were shifted upward so that each carbene C-heteroatom distance was 2 A°. This procedure initially resulted in NHC ring planes parallel to one another, as shown in panel (B) of Figure 2. In the case of the s_1 and occasionally the s_2 geometries, an additional adjustment of the initial NHC coordinates was necessary to ensure that steric repulsion between the NHCs did not result in a failure of the optimization. This involved angling the bulkier substituent groups away from one another and slightly shifting the NHC molecules apart along the heteroatom−heteroatom vector. An example of the result of this additional adjustment is shown in panel (A) of Figure 2. In all cases, the optimized geometries qualitatively resembled the initial geometries.

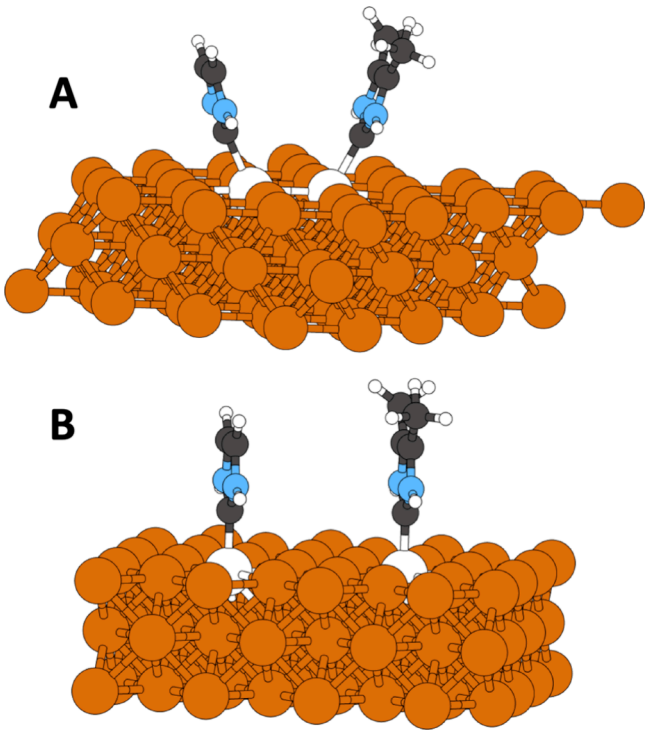

Figure 2. Cartoon representation of NHCs on SAAs that (A) did (s_1) and (B) did not (s_3) have adjustment of their initial coordinates and angles along the interheteroatom vector. Carbon/copper/hydrogen/nitrogen/palladium atoms are represented by black/orange/white/blue/white spheres, respectively.

RESULTS AND DISCUSSION

Single NHCs on SAAs. Our investigation of symmetrically substituted imidazole based NHCs bound to a variety of SAA compositions and heteroatom geometries yielded several insights. For simplicity, we first focus on the results for individual NHCs bound to SAAs of varying geometries and metal compositions. The NHC skeleton and the various substituents we investigated are shown in Figure 3. Note that while in many prior studies the nitrogen substituents are varied, based on our previous study's demonstration of the substantial steric effects on the binding affinity of the NHCs to SAAs, we have elected to modify only the less sterically significant carbon sites.[4] This allows us to focus only on the electronic influence on the NHC binding affinity. For the sake of brevity, NHCs will be designated by referencing their

https://doi.org/10.1021/acsomega.3c05376
ACS Omega 2023, 8, 37402−37412

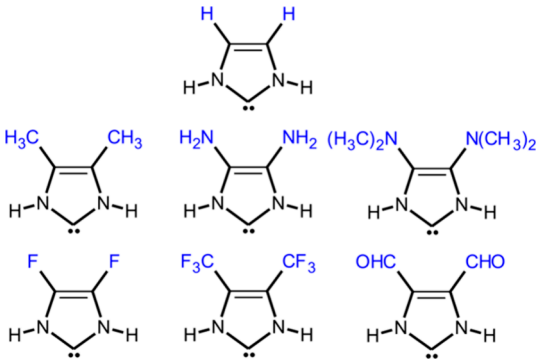

Figure 3. Skeletal structures of the NHC molecules considered in this study. Only the functional groups colored blue were varied in this study.

unique functional groups. For Cu(100)-based SAAs with individual NHCs, the coverage investigated was 0.00469 NHC molecules/$A^{\circ 2}$, where for Ag(100)-based SAAs, the coverage was 0.00361 NHC molecules/$A^{\circ 2}$ due only to the different lattice vectors. We define the binding energy BE_j for a single NHC (functional group labeled j) to a particular SAA using the energy of the gas-phase NHC $E_{NHC,j}$, the energy of the SAA surface E_{SAA}, and the energy of the NHC bound to the SAA $E_{NHC,j-SAA}$,

$$BE_j = E_{NHC,j-SAA} - E_{NHC,j} - E_{SAA} \quad (1)$$

where $BE_j < 0$ for an energetically favorable binding affinity. We will sometimes specify the SAA composition along with the index j, as in $BE_{Pd/Cu,\,j}$, but the value is still calculated using eq 1.

Nuclear magnetic resonance (NMR) of Se atoms has been utilized to quantify the π-acidity of different NHCs via Se atom chemical shielding constants obtained from NHC-selenourea adducts.[4,44−46,61,62] To quantify the connection between the EDG/EWG strength of the NHC substituents and the BE of these NHCs with the surface, the isotropic chemical shielding constant of the Se atom in an NHC-selenourea adduct (σ_j) calculated for the gas-phase NHCs with substituents labeled j from our previous study is used to create a normalized selenium atom shielding constant (Π_j) between −1 and 1.[4] The Π_j parameter gives the relative π-donor or π-acceptor strength compared to the H-substituted NHC. The formula for Π_j is,

$$\Pi_j = \frac{\sigma_j - \sigma_H}{\max(|\sigma_j - \sigma_H|)} \quad (2)$$

We have defined the unfunctionalized (only hydrogen substituents) NHC as the reference for Π_j. Therefore, $\Pi_H = 0$, which means a more EDG-substituted NHC will have $1 \geq \Pi_j > 0$ and a more EWG-substituted NHC will have $-1 \leq \Pi_j < 0$ on our relative scale. A plot of Π_j against $BE_j - BE_H$, where BE_H is the binding energy for the completely H-substituted NHC, for each SAA composition and geometry is shown in Figure 4. This relative BE correlates well with Π_j, although the aldehyde (CHO) and F groups do slightly deviate from the otherwise linear trend. NHCs substituted with EDGs have a more favorable binding affinity to the SAAs and more negative $BE_j - BE_H$. By contrast, NHCs substituted with EWGs have a weaker binding affinity to the surfaces. Both results for EDGs and EWGs are consistent with our prior work. A table of values for E_{SAA} for each SAA composition and geometry is given in Table S1, a table of σ_j, Π_j, $E_{NHC,j}$, and the BE_j values for each SAA is given in Table S2 in the Supporting Information, and the equations of fit from Figure 4 along with the relevant R^2 values are given in Table 1.

As is also clear from Figure 4, F and CH_3-substituted NHCs have noticeably decreased binding affinity to select geometries of Pd/Cu(100), Pd/Ag(100), and Pt/Cu(100) SAAs, suggesting that there is a geometric dependence of the binding affinities for certain NHCs. This preference of different geometries is quantified by using violin plots of the relative binding energies across the different geometries of each SAA for each NHC in Figure 5. The relative binding energies for the Pd/Cu(100) SAA, for example, are calculated using eq 3,

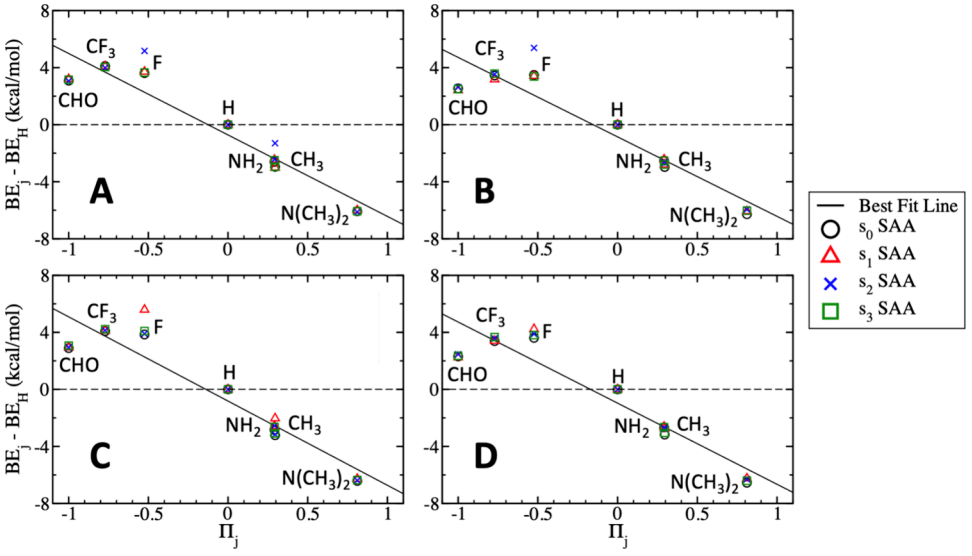

Figure 4. Plot of $BE_j - BE_H$ for various functionalized NHCs on (A) Pd/Cu(100), (B) Pd/Ag(100), (C) Pt/Cu(100), and (D) Pt/Ag(100) SAAs with various geometries against the parameter Π_j. The corresponding functional groups are listed near the relevant points. The equations of best fit and their R^2 values are given in Table 1.

https://doi.org/10.1021/acsomega.3c05376
ACS Omega 2023, 8, 37402−37412

Table 1. Linear Regression Data for the Best-Fit Lines in Figure 4, which Includes the Regression Slope (m), the y-Intercept (b), and the Coefficient of Determination (R^2) (The Regression Equation is of the Form $BE_j - BE_H = m\Pi_j + b$)

SAA composition	m (kcal/mol)	b (kcal/mol)	R^2
Pd/Cu(100)	−5.712	−0.716	0.906
Pd/Ag(100)	−5.572	−0.854	0.891
Pt/Cu(100)	−5.910	−0.818	0.890
Pt/Ag(100)	−5.692	−0.964	0.890

$$\text{relative } BE_{Pd/Cu,j} = BE_{Pd/Cu,j} - \min(BE_{Pd/Cu,j}) \quad (3)$$

where the minimum is evaluated with respect to the different possible geometries of the NHC-SAA combination. The other SAA compositions are treated analogously. Note that the violin plots were not allowed to extrapolate beyond the bounds of the data set. Interestingly, F-substituted NHCs displayed weaker binding affinities for the s_2 geometry of both Pd/Ag(100) and Pd/Cu(100) SAAs, in stark contrast to the slight preference of this geometry for all other NHCs and SAAs with Pt heteroatoms. This ubiquitous preference is why the s_2 geometry results have no variance in panels (C) and (D) of Figure 5.

The binding energy data in Table S2 also shows a different surface geometry preference (i.e., s_0 vs s_1 vs s_2 vs s_3) for Cu(100)- and Ag(100)-based SAAs depending on which metal the SAA surface is based on. To visualize this difference and its geometric dependence, violin plots of the difference of the NHC BE_j for the Ag(100)-based SAA and the Cu(100)-based SAA, which we call $\Delta BE_{Pd/Ag-Pd/Cu,j}$ or $\Delta BE_{Pt/Ag-Pt/Cu,j}$ as appropriate, are given in Figure 6. The values of $\Delta BE_{Pd/Ag-Pd/Cu,j}$ and $\Delta BE_{Pt/Ag-Pt/Cu,j}$ are calculated using eq 4a,4b,

$$\Delta BE_{Pd/Ag-Pd/Cu,j} = BE_{Pd/Ag,j} - BE_{Pd/Cu,j} \quad (4a)$$

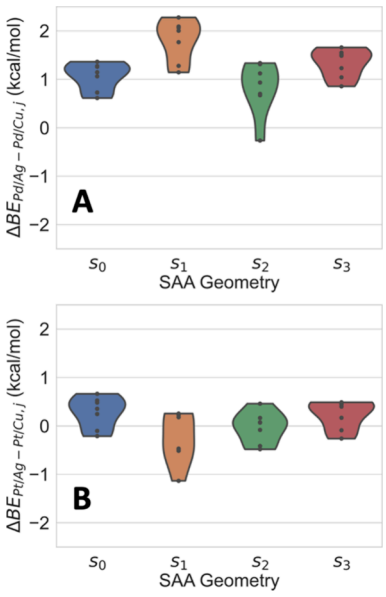

Figure 6. Violin plots of (A) $\Delta BE_{Pd/Ag-Pd/Cu,j}$ and (B) $\Delta BE_{Pt/Ag-Pt/Cu,j}$ for individual NHCs on each of the various SAA geometries.

$$\Delta BE_{Pt/Ag-Pt/Cu,j} = BE_{Pt/Ag,j} - BE_{Pt/Cu,j} \quad (4b)$$

Note that $\Delta BE_{Pd/Ag-Pd/Cu,j}$ and $\Delta BE_{Pt/Ag-Pt/Cu,j}$ are defined such that a positive value indicates a stronger binding energy to Cu(100)-based SAAs over Ag(100)-based SAAs. From Figure 6, it is apparent that there is a mild geometric dependence of $\Delta BE_{Pd/Ag-Pd/Cu,j}$. For SAAs with Pd heteroatoms, the Cu(100)-based SAAs are preferred over the Ag(100)-based surfaces by an average of 1.25 kcal/mol, though the F-substituted NHC surprisingly prefers the Ag(100)-based SAA with an s_2 geometry. By contrast, there is little meaningful geometric dependence on $\Delta BE_{Pt/Ag-Pt/Cu,j}$, and there is no significant average preference (average $\Delta BE_{Pt/Ag-Pt/Cu,j}$ = 0.05 kcal/mol) of either Cu(100) or Ag(100)-based SAAs.

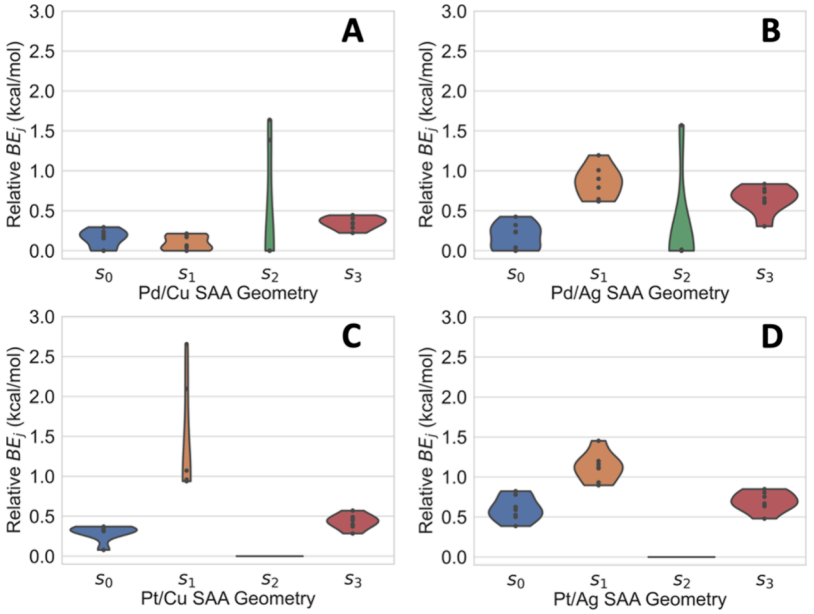

Figure 5. Violin plots of BE_j relative to the possible site geometry for each NHC bound to (A) Pd/Cu(100), (B) Pd/Ag(100), (C) Pt/Cu(100), and (D) Pt/Ag(100) SAAs calculated using eq 3. A cartoon visualization of the SAA geometries is shown in Figure 1.

https://doi.org/10.1021/acsomega.3c05376
ACS Omega 2023, 8, 37402−37412

Finally, the data in Table S2 in the Supporting Information also show a consistently stronger binding affinity of NHCs to SAAs containing Pt heteroatoms over Pd heteroatoms. This is in-line with prior work.[4] We call the difference between the BE_j values for NHCs on SAAs containing Pt heteroatoms and Pd heteroatoms $\Delta BE_{Pd/Cu-Pt/Cu,j}$ or $\Delta BE_{Pd/Ag-Pt/Ag,j}$, as appropriate. The values of $\Delta BE_{Pd/Cu-Pt/Cu,j}$ and $\Delta BE_{Pd/Ag-Pt/Ag,j}$ are calculated using eq 5a,5b,

$$\Delta BE_{Pd/Cu-Pt/Cu,j} = BE_{Pd/Cu,j} - BE_{Pt/Cu,j} \quad (5a)$$

$$\Delta BE_{Pd/Ag-Pt/Ag,j} = BE_{Pd/Ag,j} - BE_{Pt/Ag,j} \quad (5b)$$

By convention, $\Delta BE_{Pd/Cu-Pt/Cu,j} > 0$ and $\Delta BE_{Pd/Ag-Pt/Ag,j} > 0$ when a the NHC has a stronger binding affinity to the SAA with a Pt heteroatom. NHCs bind to Cu(100)-based SAAs an average of 8.38 kcal/mol stronger with a Pt heteroatom than a Pd heteroatom, while Ag(100)-based SAAs yield an average of 9.59 kcal/mol stronger binding. This effect is somewhat geometry dependent for a small subset of NHCs, which we show using the violin plots in Figure 7. The geometric

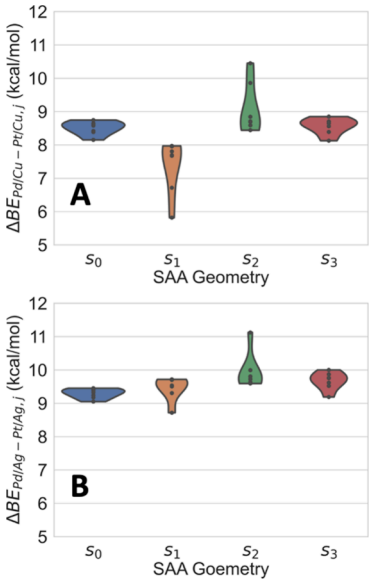

Figure 7. Violin plots of (A) $\Delta BE_{Pd/Cu-Pt/Cu,j}$ and (B) $\Delta BE_{Pd/Ag-Pt/Ag,j}$ for individual NHCs on each of the various SAA geometries.

dependence for Cu(100)-based SAAs is significant only for F and CH_3-substituted NHCs, while for Ag(100)-based SAAs only F-substituted NHCs show any significant geometric dependence.

Paired NHCs on SAAs. In this section, we will explore the effect of adding another NHC to the simulation cell. For Cu(100)-based SAAs with pairs of NHCs, the coverage investigated was 0.00938 NHC molecules/$A^{\circ 2}$, where for Ag(100)-based SAAs, the coverage was 0.00721 NHC molecules/$A^{\circ 2}$ due once again to the different lattice vectors. The identity of the electronic substituents around the NHC ring makes a pronounced difference in the relative binding affinity of a pair of NHCs with an SAA surface. To quantify this, we use the Se-NMR chemical shielding constant Π_j from eq 2 for each species to create a paired donor−acceptor parameter $\Pi_{j,k} = \Pi_j + \Pi_k$, where j and k are indices for the NHCs with different substituents. The parameter $\Pi_{j,k}$ scales with the net relative donor and acceptor strengths of the two NHCs' substituents. Note that $\Pi_{j,k}$ measures the net donor and acceptor strengths as if the two NHCs were independent, which will allow us to determine if this is the case when the NHCs are paired on the surface. The paired NHC-SAA binding energy $BE_{j,k}$ is quantified using the difference in the energy of the pair of NHCs on the surface $E_{NHC,j-NHC,k-SAA}$, the SAA surface energy E_{SAA}, and the energies of the individual NHCs $E_{NHC,j}$ and $E_{NHC,k}$, respectively,

$$BE_{j,k} = E_{NHC,j-NHC,k-SAA} - E_{SAA} - E_{NHC,j} - E_{NHC,k} \quad (6)$$

Once again, we will sometimes specify the identity of the SAA, as in $BE_{Pd/Cu,j,k}$, though eq 6 will still be used. Pairs of EDG-substituted NHCs and a mixture of EDG/EWG-substituted NHCs have generally stronger binding to the surface than the pair of H-substituted NHCs. The magnitude of this effect scales roughly linearly with $\Pi_{j,k}$, often even when $\Pi_{j,k} < 0$. The latter result is somewhat surprising since individual EWG NHCs exclusively had weaker binding affinities when compared to the H-substituted NHC across all SAA geometries and compositions. This suggests that the pairing of NHCs on the surface may typically strengthen the BE when compared to the individual NHCs. By contrast, pairs of EWG-substituted NHCs always had weaker binding affinity compared to the pair of H-substituted NHCs, as expected. This behavior is shown in detail in Figure 8 and linear regression data from the best-fit lines are given in Table 2.

The dependence of the paired NHC binding energy on the surface geometry is shown in Figure 8. It is, however, somewhat obscured, so in Figure 9 we visualize how $BE_{j,k}$ varies relative to the geometry using violin plots. As before, the relative binding energies for the Pd/Cu(100) SAA, for example, are calculated using eq 7,

$$\text{relative } BE_{Pd/Cu,j,k} = BE_{Pd/Cu,j,k} - \min(BE_{Pd/Cu,j,k}) \quad (7)$$

where the minimum is evaluated with respect to the different possible heteroatom geometries of the NHC-NHC-SAA combination. We find that in most cases, the s_2 geometry is the most stable for pairs of NHCs. Only the Pt/Ag(100) SAA gave a preference for the s_2 geometry in every case, although it was preferred in the vast majority of cases for the other SAA compositions. This geometric preference is why there is no variance for the s_2 results in panel (D) of Figure 9. The geometric preference of pairs of NHCs is often quite pronounced and may have significant implications for the clustering of NHCs on heteroatom "islands" on SAA surfaces.[13]

When pairs of NHCs were bound to s_1, s_2, and s_3 SAA geometries, there was a geometrically dependent effect on the relative binding affinity compared to that of the individual NHCs on the same surface. To quantify this, we define the difference in the paired and unpaired NHC BE, ΔBE_{p-up}, using the paired NHC-SAA $BE_{j,k}$ and the individual NHC-SAA BE_js,

$$\Delta BE_{p-up} = BE_{j,k} - BE_j - BE_k \quad (8)$$

where the subscript $p-up$ stands for the difference of paired and unpaired NHC-SAA BEs. Violin plots of ΔBE_{p-up} for the various SAAs compositions and surface geometries are given in Figure 10, and a full accounting of the data for $\Pi_{j,k}$, $BE_{j,k}$, and ΔBE_{p-up} is given in Tables S3−S14 of the Supporting Information. In many cases, the binding affinity to the SAA of the NHC pair was more energetically favorable relative to

https://doi.org/10.1021/acsomega.3c05376
ACS Omega 2023, 8, 37402−37412

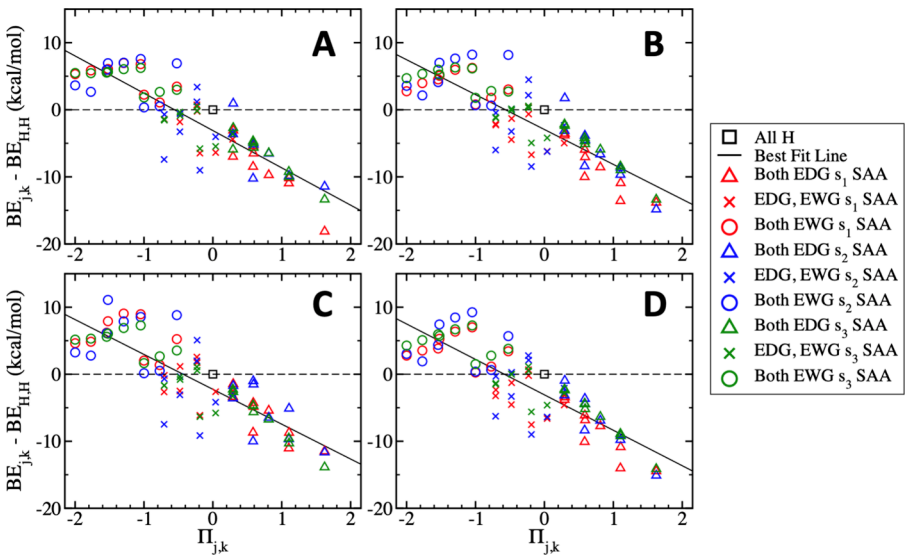

Figure 8. Plot of $BE_{j,k} - BE_{H,H}$ for NHCs on (A) Pd/Cu(100), (B) Pd/Ag(100), (C) Pt/Cu(100), and (D) Pt/Ag(100) SAAs against the combined relative Se-NMR shielding parameter $\Pi_{j,k}$ with markers and colors differentiating both the SAA geometry and the classes of NHC substituents. The equations of best fit and their R^2 values are given in Table 2.

Table 2. Linear Regression Data for the Best-Fit Lines Shown in Figure 8 (the Regression Equation is of the Form $BE_{j,k} - BE_{H,H} = m\Pi_{j,\text{and } k} + b$)

SAA composition	m (kcal/mol)	b (kcal/mol)	R^2
Pd/Cu(100)	−5.559	−3.102	0.777
Pd/Ag(100)	−5.202	−2.945	0.732
Pt/Cu(100)	−5.202	−2.245	0.697
Pt/Ag(100)	−5.289	−3.074	0.726

the individual NHCs bound to the SAA, giving $\Delta BE_{p-up} < 0$, though there were exceptions. Most notably, the average ΔBE_{p-up} for a Pt/Cu(100) SAA was slightly positive for every geometry studied, suggesting that NHCs are resistant to pairing on this surface on average, which could have pronounced effects for molecules aggregating on this SAA. By contrast, only the Pd/Ag(100) surface had negative average ΔBE_{p-up} values for every surface geometry, suggesting that this SAA composition encourages aggregation of NHCs on average. For the Pd/Cu(100) and Pt/Ag(100) SAAs, only the s_2 geometry had a negative average ΔBE_{p-up} value, suggesting that there is a favored distance between heteroatoms that encourages the pairing of NHCs. While the average ΔBE_{p-up} values are not particularly large, they have many large-magnitude values that suggest that there are significant geometric effects that may become important depending on

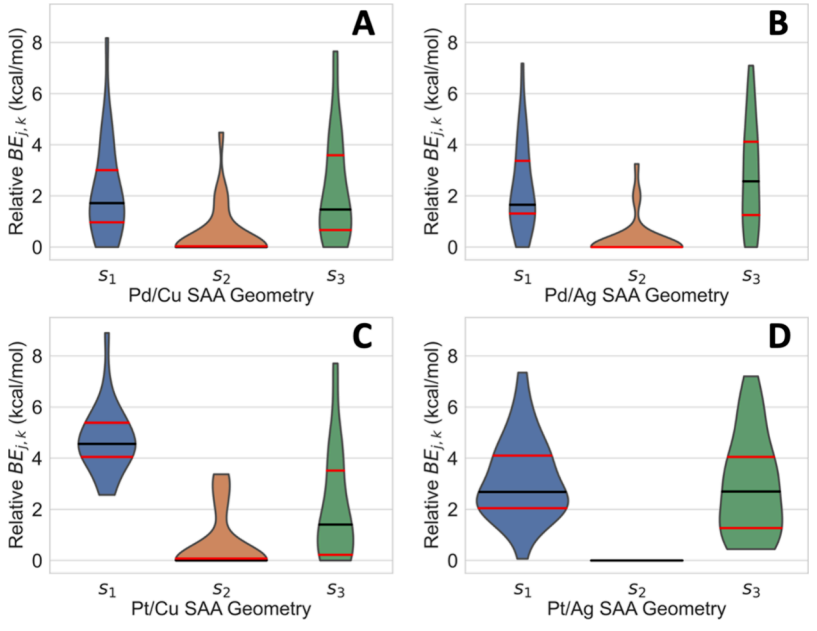

Figure 9. Violin plots of the geometrically relative $BE_{j,k}$ value from eq 7 for pairs of NHCs bound to each SAA composition ((A) Pd/Cu(100), (B) Pd/Ag(100), (C) Pt/Cu(100), and (D) Pt/Ag(100)) and geometry. Red horizontal lines correspond to the first and third quartiles, while the black lines are the medians of the data sets.

https://doi.org/10.1021/acsomega.3c05376
ACS Omega 2023, 8, 37402−37412

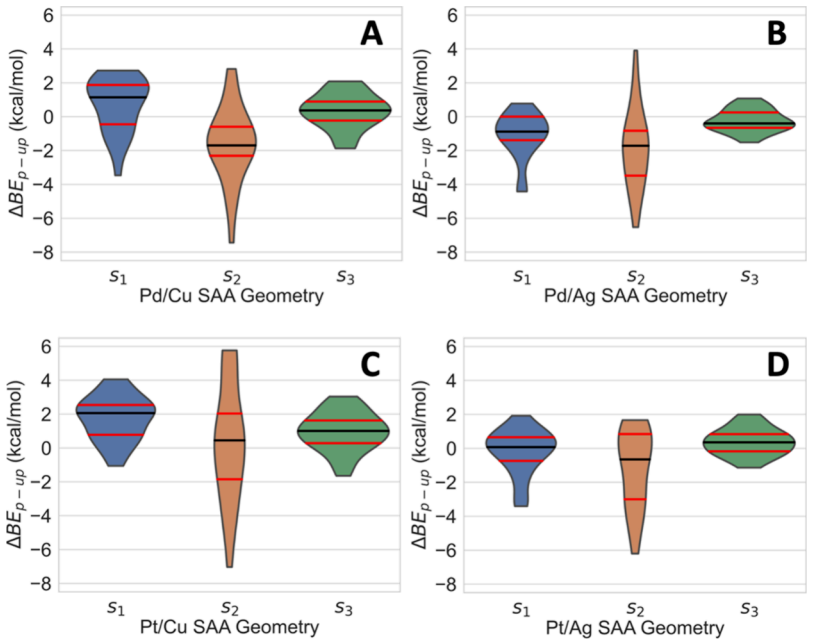

Figure 10. Violin plots of ΔBE_{p-up} for the various NHCs across SAA composed of (A) Pd/Cu(100), (B) Pd/Ag(100), (C) Pt/Cu(100), and (D) Pt/Ag(100) with various geometries. The red lines represent the first and third quartiles, and the black line represents the median of the distribution.

the choice of NHCs and SAAs. The value of ΔBE_{p-up} is not meaningfully correlated with the electronic parameter $\Pi_{j,k}$, as shown in Figure 11 and quantified in Table 3. This means that

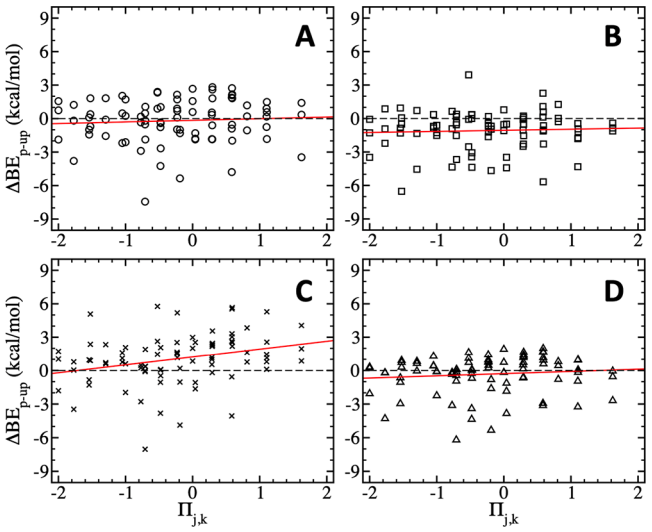

Figure 11. Plots of ΔBE_{p-up} vs $\Pi_{j,k}$ for the various NHCs bound to SAAs composed of A. Pd/Cu(100) B. Pd/Ag(100) C. Pt/Cu(100) and D. Pt/Ag(100) with various geometries, with distinct symbols for each SAA composition. The red lines represent the line of best fit, the statistics of which are given in Table 3.

the effect is not intrinsically linked to the electronics of the free NHC and must have some underlying cooperative mechanism involving the surface and steric repulsion of the NHC molecules.

As with the individual NHCs bound to SAA surfaces, there is an average preference of SAA compositions based on Cu(100) when the surface has a Pd heteroatom. By contrast, there is an average preference for Ag(100)-based SAAs when

Table 3. Linear Regression Data for the Best-Fit Lines Are Shown in Figure 11 (the Regression Equation is of the Form $\Delta BE_{p-up} = m\Pi_{j,k} + b$)

SAA composition	m (kcal/mol)	b (kcal/mol)	R^2
Pd/Cu(100)	0.147	−0.151	0.005
Pd/Ag(100)	0.100	−1.055	0.003
Pt/Cu(100)	0.710	1.215	0.081
Pt/Ag(100)	0.197	0.281	0.011

there is a Pt heteroatom. This is quantified by taking the difference between $BE_{j,k}$ values for the same NHC pair on surfaces made from Cu(100) or Ag(100) with either the Pd or Pt heteroatoms, which we call $\Delta BE_{Pd/Ag-Pd/Cu,j,k}$ or $\Delta BE_{Pt/Ag-Pt/Cu,j,k}$ as appropriate. The values of $\Delta BE_{Pd/Ag-Pd/Cu,j,k}$ and $\Delta BE_{Pt/Ag-Pt/Cu,j,k}$ are calculated using eq 9a,9b,

$$\Delta BE_{Pd/Ag-Pd/Cu,j,k} = BE_{Pd/Ag,j,k} - BE_{Pd/Cu,j,k} \quad (9a)$$

$$\Delta BE_{Pt/Ag-Pt/Cu,j,k} = BE_{Pt/Ag,j,k} - BE_{Pt/Cu,j,k} \quad (9b)$$

By convention, a positive value of $\Delta BE_{Pd/Ag-Pd/Cu,j,k}$ or $\Delta BE_{Pt/Ag-Pt/Cu,j,k}$ indicates that Cu(100)-based SAA yields a greater binding affinity for the NHCs. As can be seen in Figure 12, there is little geometric dependence of this effect for SAAs with Pd heteroatoms, although there are significant outliers. Specifically, systems involving H & NH_2-substituted NHCs, two $N(CH_3)_2$-substituted NHCs, and CF_3 & $N(CH_3)_2$-substituted NHCs were responsible for the most significant outliers in panel A of Figure 12. There is some noteworthy geometric dependence on the preference of Ag(100)-based SAAs with Pt heteroatoms, with the preference for Ag(100)-based SAAs increasing as the site spacing decreases.

Finally, pairs of NHCs have a stronger binding affinity to SAA surfaces with Pt heteroatoms over those with Pd heteroatoms. This is quantified using the difference between $BE_{j,k}$ values for the same NHC pair on surfaces made from with

https://doi.org/10.1021/acsomega.3c05376
ACS Omega 2023, 8, 37402−37412

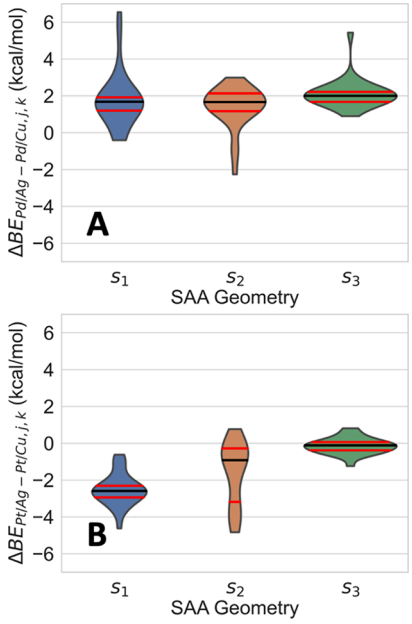

Figure 12. Violin plots of (A) $\Delta BE_{Pd/Ag-Pd/Cu,j,k}$ and (B) $\Delta BE_{Pt/Ag-Pt/Cu,j,k}$ for pairs of NHCs on each of the various SAA geometries.

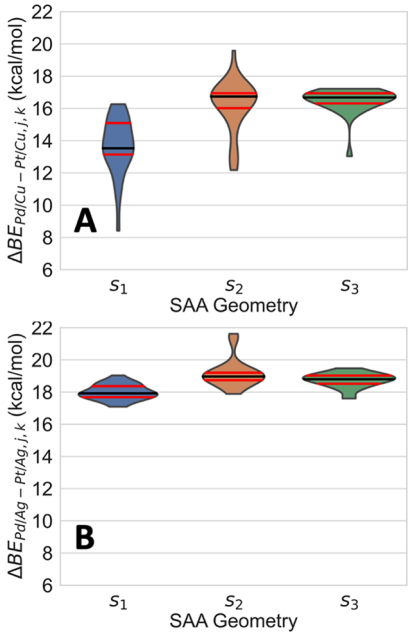

Figure 13. Violin plots of (A) $\Delta BE_{Pd/Cu-Pt/Cu,j,k}$ and (B) $\Delta BE_{Pd/Ag-Pt/Ag,j,k}$ for pairs of NHCs on each of the various SAA geometries.

either the Pd or Pt heteroatoms for a given SAA composition, which we call $\Delta BE_{Pd/Cu-Pt/Cu,j,k}$ or $\Delta BE_{Pd/Ag-Pt/Ag,j,k}$ as appropriate. The values of $\Delta BE_{Pd/Cu-Pt/Cu,j,k}$ and $\Delta BE_{Pd/Ag-Pt/Ag,j,k}$ are calculated using eq 10a,10b,

$$\Delta BE_{Pd/Cu-Pt/Cu,j,k} = BE_{Pd/Cu,j,k} - BE_{Pt/Cu,j,k} \quad (10a)$$

$$\Delta BE_{Pd/Ag-Pt/Ag,j,k} = BE_{Pd/Ag,j,k} - BE_{Pt/Ag,j,k} \quad (10b)$$

For Cu(100)-based SAAs, there is a weaker preference for Pt heteroatoms in the s_1 geometry, while the s_2 and s_3 geometries are quite similar. By contrast, there is very little dependence of $\Delta BE_{Pd/Ag-Pt/Ag,j,k}$ on the geometries of Ag(100)-based SAAs. This is shown in Figure 13.

CONCLUSIONS

We have conducted nonlocal periodic density functional theory (DFT) calculations of N-heterocyclic carbenes (NHCs) adsorbed to Pd/Cu(100), Pt/Cu(100), Pd/Ag(100), and Pt/Ag(100) single atom alloys. We predict that NHCs with electron donating groups (EDGs) have a stronger binding affinity to the SAA surface compared with NHCs functionalized with electron withdrawing groups (EWGs).

When considering the dispersity of Pd or Pt atoms on the Cu(100) or the Ag(100) surface, it was predicted that NHCs typically preferentially bind to SAAs with geometries containing a small space between the heteroatom sites, which we call the s_2 geometry. This pattern is predicted to persist whether a single NHC or a pair of NHCs is bound to the SAA, though there were sporadic cases where this geometry was not favored. We predict that this has serious implications for the clustering of NHC molecules in ways specific to the SAA surface geometry and the breadth of conditions that thermodynamically induce desorption of the NHC molecular cork.

This study further illustrates that there are approximately linear relationships between independent NMR-based parameters measuring the electron donating and withdrawing character of the NHCs and their binding energies to SAAs of various compositions. This indicates that the strongly tunable electronics of NHCs can be exploited to control the conditions under which NHCs may act as viable molecular corks. This study also predicts that there is a surface-dependent and geometry-dependent tendency to enhance or weaken the binding of NHCs to the surface when they aggregate with one another, with the Pd/Ag(100) SAA most consistently strengthening and the Pt/Cu(100) SAA most consistently weakening the binding.

ASSOCIATED CONTENT

Supporting Information

The Supporting Information is available free of charge at https://pubs.acs.org/doi/10.1021/acsomega.3c05376.

Tabulated values of E_{SAA} for each distinct SAA composition and geometry, the values of $E_{NHC,j}$, σ_j, and Π_j for each NHC studied, BE_j for every singular NHC-SAA combination studied, and $\Pi_{j,k}$, $BE_{j,k}$, and $\Delta BE_{j,k}$ for each NHC pair-SAA combination studied (PDF)

Unoptimized *XYZ* coordinates built from the optimized SAA surface and NHC gas-phase coordinates and fully optimized POSCAR files for each NHC-SAA system studied; gas-phase NHC coordinates and bare SAA surface coordinates can be extracted from the *XYZ* files, if desired (ZIP)

AUTHOR INFORMATION

Corresponding Authors

Matthew D. Hanson − *Department of Chemistry, Le Moyne College, Syracuse, New York 13214, United States;* orcid.org/0000-0001-8463-0672; Email: hansoma@lemoyne.edu

https://doi.org/10.1021/acsomega.3c05376
ACS Omega 2023, 8, 37402−37412

Scott M. Simpson − *Department of Chemistry, St. Bonaventure University, St. Bonaventure, New York 14778, United States;* orcid.org/0000-0001-8093-1814; Email: ssimpson@sbu.edu

Complete contact information is available at: https://pubs.acs.org/10.1021/acsomega.3c05376

Notes

The authors declare no competing financial interest.

■ ACKNOWLEDGMENTS

S.S. acknowledges the National Science Foundation (Award #2142874) for support of this research and the Donors of the American Chemical Society Petroleum Research Fund (PRF-58954-UNI5). M.H. acknowledges the National Science Foundation (Award #2142874) for support of this research.

■ REFERENCES

(1) Abe, J. O.; Popoola, A. P. I.; Ajenifuja, E.; Popoola, O. M. Hydrogen Energy, Economy and Storage: Review and Recommendation. *Int. J. Hydrogen Energy* **2019**, *44* (29), 15072−15086.

(2) Schneemann, A.; White, J. L.; Kang, S.; Jeong, S.; Wan, L. F.; Cho, E. S.; Heo, T. W.; Prendergast, D.; Urban, J. J.; Wood, B. C.; Allendorf, M. D.; Stavila, V. Nanostructured Metal Hydrides for Hydrogen Storage. *Chem. Rev.* **2018**, *118* (22), 10775−10839.

(3) Marcinkowski, M. D.; Jewell, A. D.; Stamatakis, M.; Boucher, M. B.; Lewis, E. A.; Murphy, C. J.; Kyriakou, G.; Sykes, E. C. H. Controlling a Spillover Pathway with the Molecular Cork Effect. *Nat. Mater.* **2013**, *12* (6), 523−528.

(4) Simpson, S. The Search for Molecular Corks beyond Carbon Monoxide: A Quantum Mechanical Study of N-Heterocyclic Carbene Adsorption on Pd/Cu(100) and Pt/Cu(100) Single Atom Alloys. *JCIS Open* **2021**, *3*, No. 100013.

(5) Darby, M. T.; Lucci, F. R.; Marcinkowski, M. D.; Therrien, A. J.; Michaelides, A.; Stamatakis, M.; Sykes, E. C. H. Carbon Monoxide Mediated Hydrogen Release from PtCu Single-Atom Alloys: The Punctured Molecular Cork Effect. *J. Phys. Chem. C* **2019**, *123* (16), 10419−10428.

(6) Cheng, N.; Zhang, L.; Doyle-Davis, K.; Sun, X. Single-Atom Catalysts: From Design to Application. *Electrochem. Energy Rev.* **2019**, *2* (4), 539−573.

(7) Hannagan, R. T.; Giannakakis, G.; Flytzani-Stephanopoulos, M.; Sykes, E. C. H. Single-Atom Alloy Catalysis. *Chem. Rev.* **2020**, *120* (21), 12044−12088.

(8) Lee, J. D.; Qi, Z.; Foucher, A. C.; Ngan, H. T.; Dennis, K.; Cui, J.; Sadykov, I. I.; Crumlin, E. J.; Sautet, P.; Stach, E. A.; Friend, C. M.; Madix, R. J.; Biener, J. Facilitating Hydrogen Dissociation over Dilute Nanoporous Ti−Cu Catalysts. *J. Am. Chem. Soc.* **2022**, *144* (37), 16778−16791.

(9) Lucci, F. R.; Marcinkowski, M. D.; Lawton, T. J.; Sykes, E. C. H. H_2 Activation and Spillover on Catalytically Relevant Pt−Cu Single Atom Alloys. *J. Phys. Chem. C* **2015**, *119* (43), 24351−24357.

(10) Luneau, M.; Lim, J. S.; Patel, D. A.; Sykes, E. C. H.; Friend, C. M.; Sautet, P. Guidelines to Achieving High Selectivity for the Hydrogenation of α,β-Unsaturated Aldehydes with Bimetallic and Dilute Alloy Catalysts: A Review. *Chem. Rev.* **2020**, *120* (23), 12834−12872.

(11) Osada, W.; Tanaka, S.; Mukai, K.; Kawamura, M.; Choi, Y.; Ozaki, F.; Ozaki, T.; Yoshinobu, J. Elucidation of the Atomic-Scale Processes of Dissociative Adsorption and Spillover of Hydrogen on the Single Atom Alloy Catalyst Pd/Cu(100). *Phys. Chem. Chem. Phys.* **2022**, *24* (36), 21705−21713.

(12) Zhao, G.-C.; Qiu, Y.-Q.; Liu, C.-G. A Systematic Theoretical Study of Hydrogen Activation, Spillover and Desorption in Single-Atom Alloys. *Appl. Catal. A: Gen.* **2021**, *610*, No. 117948.

(13) O'Connor, C. R.; Duanmu, K.; Patel, D. A.; Muramoto, E.; van Spronsen, M. A.; Stacchiola, D.; Sykes, E. C. H.; Sautet, P.; Madix, R. J.; Friend, C. M. Facilitating Hydrogen Atom Migration via a Dense Phase on Palladium Islands to a Surrounding Silver Surface. *Proc. Natl. Acad. Sci. U.S.A.* **2020**, *117* (37), 22657−22664.

(14) Anger, G.; Winkler, A.; Rendulic, K. D. Adsorption and Desorption Kinetics in the Systems H2/Cu(100), H2/Cu(110) and H2/Cu(100). *Surf. Sci.* **1989**, *220* (1), 1−17.

(15) Cheng, H.; Chen, L.; Cooper, A. C.; Sha, X.; Pez, G. P. Hydrogen Spillover in the Context of Hydrogen Storage Using Solid-State Materials. *Energy Environ. Sci.* **2008**, *1* (3), 338.

(16) Lewis, E. A.; Marcinkowski, M. D.; Murphy, C. J.; Liriano, M. L.; Sykes, E. C. H. Hydrogen Dissociation, Spillover, and Desorption from Cu-Supported Co Nanoparticles. *J. Phys. Chem. Lett.* **2014**, *5* (19), 3380−3385.

(17) Lucci, F. R.; Darby, M. T.; Mattera, M. F. G.; Ivimey, C. J.; Therrien, A. J.; Michaelides, A.; Stamatakis, M.; Sykes, E. C. H. Controlling Hydrogen Activation, Spillover, and Desorption with Pd−Au Single-Atom Alloys. *J. Phys. Chem. Lett.* **2016**, *7* (3), 480−485.

(18) Simonovis, J. P.; Hunt, A.; Senanayake, S. D.; Waluyo, I. Subtle and Reversible Interactions of Ambient Pressure H_2 with Pt/Cu(100) Single-Atom Alloy Surfaces. *Surf. Sci.* **2019**, *679*, 207−213.

(19) Réocreux, R.; Kress, P. L.; Hannagan, R. T.; Çınar, V.; Stamatakis, M.; Sykes, E. C. H. Controlling Hydrocarbon (De)-Hydrogenation Pathways with Bifunctional PtCu Single-Atom Alloys. *J. Phys. Chem. Lett.* **2020**, *11* (20), 8751−8757.

(20) Chen, W.; Wei, T.; Wang, D.; Zhao, Y. Effect of Elemental Doping on the Adsorption Behavior and the Mechanism of Hydrogen Adsorption on the Zirconium Surface. *J. Phys. Chem. C* **2022**, *126* (37), 15944−15951.

(21) Kyriakou, G.; Davidson, E. R. M.; Peng, G.; Roling, L. T.; Singh, S.; Boucher, M. B.; Marcinkowski, M. D.; Mavrikakis, M.; Michaelides, A.; Sykes, E. C. H. Significant Quantum Effects in Hydrogen Activation. *ACS Nano* **2014**, *8* (5), 4827−4835.

(22) Hirscher, M.; Yartys, V. A.; Baricco, M.; Bellosta von Colbe, J.; Blanchard, D.; Bowman, R. C.; Broom, D. P.; Buckley, C. E.; Chang, F.; Chen, P.; Cho, Y. W.; Crivello, J. C.; Cuevas, F.; David, W. I. F.; de Jongh, P. E.; Denys, R. V.; Dornheim, M.; Felderhoff, M.; Filinchuk, Y.; Froudakis, G. E.; Grant, D. M.; Gray, E. M.; Hauback, B. C.; He, T.; Humphries, T. D.; Jensen, T. R.; Kim, S.; Kojima, Y.; Latroche, M.; Li, H. W.; Lototskyy, M. V.; Makepeace, J. W.; Møller, K. T.; Naheed, L.; Ngene, P.; Noréus, D.; Nygård, M. M.; Orimo, S. i.; Paskevicius, M.; Pasquini, L.; Ravnsbæk, D. B.; Veronica Sofianos, M.; Udovic, T. J.; Vegge, T.; Walker, G. S.; Webb, C. J.; Weidenthaler, C.; Zlotea, C. Materials for Hydrogen-Based Energy Storage − Past, Recent Progress and Future Outlook. *J. Alloys Compd.* **2020**, *827*, No. 153548.

(23) Tierney, H. L.; Baber, A. E.; Kitchin, J. R.; Sykes, E. C. H. Hydrogen Dissociation and Spillover on Individual Isolated Palladium Atoms. *Phys. Rev. Lett.* **2009**, *103* (24), No. 246102.

(24) Réocreux, R.; Sykes, E. C. H.; Michaelides, A.; Stamatakis, M. Stick or Spill? Scaling Relationships for the Binding Energies of Adsorbates on Single-Atom Alloy Catalysts. *J. Phys. Chem. Lett.* **2022**, *13* (31), 7314−7319.

(25) Ernst, J. B.; Muratsugu, S.; Wang, F.; Tada, M.; Glorius, F. Tunable Heterogeneous Catalysis: N-Heterocyclic Carbenes as Ligands for Supported Heterogeneous Ru/K-Al_2O_3 Catalysts To Tune Reactivity and Selectivity. *J. Am. Chem. Soc.* **2016**, *138* (34), 10718−10721.

(26) Goodman, E. D.; Johnston-Peck, A. C.; Dietze, E. M.; Wrasman, C. J.; Hoffman, A. S.; Abild-Pedersen, F.; Bare, S. R.; Plessow, P. N.; Cargnello, M. Catalyst Deactivation via Decomposition into Single Atoms and the Role of Metal Loading. *Nat. Catal* **2019**, *2* (9), 748−755.

(27) Ikemoto, S.; Muratsugu, S.; Koitaya, T.; Tsuji, Y.; Das, M.; Yoshizawa, K.; Glorius, F.; Tada, M. Coordination-Induced Trigger for Activity: N-Heterocyclic Carbene-Decorated Ceria Catalysts Incorporating Cr and Rh with Activity Induction by Surface Adsorption Site Control. *J. Am. Chem. Soc.* **2023**, *145* (3), 1497−1504.

(28) Jiang, Y.; Fei, H. N-Heterocyclic Carbene-Ligated Metal Complexes and Clusters for Photocatalytic CO $_2$ Reduction. *Inorg. Chem. Front.* **2023**, 4313.
(29) Ouyang, M.; Papanikolaou, K. G.; Boubnov, A.; Hoffman, A. S.; Giannakakis, G.; Bare, S. R.; Stamatakis, M.; Flytzani-Stephanopoulos, M.; Sykes, E. C. H. Directing Reaction Pathways via in Situ Control of Active Site Geometries in PdAu Single-Atom Alloy Catalysts. *Nat. Commun.* **2021**, *12* (1), 1549.
(30) Pédeutour, J.-N.; Radhakrishnan, K.; Cramail, H.; Deffieux, A. Reactivity of Metallocene Catalysts for Olefin Polymerization: Influence of Activator Nature and Structure. *Macromol. Rapid Commun.* **2001**, *22* (14), 1095.
(31) Scholten, J. D.; Ebeling, G.; Dupont, J. On the Involvement of NHC Carbenes in Catalytic Reactions by Iridium Complexes, Nanoparticle and Bulk Metal Dispersed in Imidazolium Ionic Liquids. *Dalton Trans.* **2007**, *47*, 5554.
(32) Kyriakou, G.; Boucher, M. B.; Jewell, A. D.; Lewis, E. A.; Lawton, T. J.; Baber, A. E.; Tierney, H. L.; Flytzani-Stephanopoulos, M.; Sykes, E. C. H. Isolated Metal Atom Geometries as a Strategy for Selective Heterogeneous Hydrogenations. *Science* **2012**, *335* (6073), 1209−1212.
(33) Boucher, M. B.; Zugic, B.; Cladaras, G.; Kammert, J.; Marcinkowski, M. D.; Lawton, T. J.; Sykes, E. C. H.; Flytzani-Stephanopoulos, M. Single Atom Alloy Surface Analogs in Pd0.18Cu15 Nanoparticles for Selective Hydrogenation Reactions. *Phys. Chem. Chem. Phys.* **2013**, *15* (29), 12187.
(34) Papanikolaou, K. G.; Darby, M. T.; Stamatakis, M. CO-Induced Aggregation and Segregation of Highly Dilute Alloys: A Density Functional Theory Study. *J. Phys. Chem. C* **2019**, *123* (14), 9128−9138.
(35) Lucci, F. R.; Zhang, L.; Thuening, T.; Uhlman, M. B.; Schilling, A. C.; Henkelman, G.; Sykes, Charles H.; E. The Effect of Single Pd Atoms on the Energetics of Recombinative O2 Desorption from Au(100). *Surf. Sci.* **2018**, *677*, 296−300.
(36) Gao, F.; Wang, Y.; Goodman, D. W. CO Oxidation over AuPd(100) from Ultrahigh Vacuum to Near-Atmospheric Pressures: The Critical Role of Contiguous Pd Atoms. *J. Am. Chem. Soc.* **2009**, *131* (16), 5734−5735.
(37) Crudden, C. M.; Horton, J. H.; Ebralidze, I. I.; Zenkina, O. V.; McLean, A. B.; Drevniok, B.; She, Z.; Kraatz, H.-B.; Mosey, N. J.; Seki, T.; Keske, E. C.; Leake, J. D.; Rousina-Webb, A.; Wu, G. Ultra Stable Self-Assembled Monolayers of N-Heterocyclic Carbenes on Gold. *Nat. Chem.* **2014**, *6* (5), 409−414.
(38) Crudden, C. M.; Horton, J. H.; Narouz, M. R.; Li, Z.; Smith, C. A.; Munro, K.; Baddeley, C. J.; Larrea, C. R.; Drevniok, B.; Thanabalasingam, B.; McLean, A. B.; Zenkina, O. V.; Ebralidze, I. I.; She, Z.; Kraatz, H.-B.; Mosey, N. J.; Saunders, L. N.; Yagi, A. Simple Direct Formation of Self-Assembled N-Heterocyclic Carbene Monolayers on Gold and Their Application in Biosensing. *Nat. Commun.* **2016**, *7* (1), 12654.
(39) Larrea, C. R.; Baddeley, C. J.; Narouz, M. R.; Mosey, N. J.; Horton, J. H.; Crudden, C. M. *N* -Heterocyclic Carbene Self-Assembled Monolayers on Copper and Gold: Dramatic Effect of Wingtip Groups on Binding, Orientation and Assembly. *ChemPhysChem* **2017**, *18* (24), 3536−3539.
(40) Smith, C. A.; Narouz, M. R.; Lummis, P. A.; Singh, I.; Nazemi, A.; Li, C.-H.; Crudden, C. M. *N*-Heterocyclic Carbenes in Materials Chemistry. *Chem. Rev.* **2019**, *119* (8), 4986−5056.
(41) Dominique, N. L.; Chen, R.; Santos, A. V. B.; Strausser, S. L.; Rauch, T.; Kotseos, C. Q.; Boggess, W. C.; Jensen, L.; Jenkins, D. M.; Camden, J. P. Ad Aurum: Tunable Transfer of N-Heterocyclic Carbene Complexes to Gold Surfaces. *Inorg. Chem. Front.* **2022**, *9* (23), 6279−6287.
(42) Barnett, C.; Cole, M. L.; Harper, J. B. The Core Difference between a Mesoionic and a Normal *N*-Heterocyclic Carbene. *ACS Omega* **2022**, *7* (38), 34657−34664.
(43) Barnett, C.; Cole, M. L.; Harper, J. B. Steric Properties of *N* -Heterocyclic Carbenes Affect the Performance of Electronic Probes. *Eur. J. Inorg. Chem.* **2021**, *2021* (47), 4954−4958.
(44) Barnett, C.; Cole, M. L.; Harper, J. B. A Dual NMR Probe Approach to Understanding the Electronic Properties of *N* -Heterocyclic Carbenes. *Chem. Methods* **2021**, *1* (8), 374−381.
(45) Bernhammer, J. C.; Frison, G.; Huynh, H. V. Electronic Structure Trends in N-Heterocyclic Carbenes (NHCs) with Varying Number of Nitrogen Atoms and NHC—Transition-Metal Bond Properties. *Chem. - Eur. J.* **2013**, *19* (38), 12892−12905.
(46) Barnett, C.; Harper, J. B.; Cole, M. L. Correlating Electronic Properties of *N*-Heterocyclic Carbenes with Structure, and the Implications of Using Different Probes. *ChemistrySelect* **2022**, *7* (2), No. e202104348, DOI: 10.1002/slct.202104348.
(47) Dorta, R.; Stevens, E. D.; Scott, N. M.; Costabile, C.; Cavallo, L.; Hoff, C. D.; Nolan, S. P. Steric and Electronic Properties of N-Heterocyclic Carbenes (NHC): A Detailed Study on Their Interaction with $Ni(CO)_4$. *J. Am. Chem. Soc.* **2005**, *127* (8), 2485−2495.
(48) Blöchl, P. E. Projector Augmented-Wave Method. *Phys. Rev. B* **1994**, *50* (24), 17953−17979.
(49) Kresse, G.; Joubert, D. From Ultrasoft Pseudopotentials to the Projector Augmented-Wave Method. *Phys. Rev. B* **1999**, *59* (3), 1758−1775.
(50) Klimeš, J.; Bowler, D. R.; Michaelides, A. Chemical Accuracy for the van Der Waals Density Functional. *J. Phys.: Condens. Matter* **2010**, *22* (2), No. 022201.
(51) Klimeš, J.; Bowler, D. R.; Michaelides, A. Van Der Waals Density Functionals Applied to Solids. *Phys. Rev. B* **2011**, *83* (19), 195131.
(52) Kresse, G.; Furthmüller, J. Efficiency of Ab-Initio Total Energy Calculations for Metals and Semiconductors Using a Plane-Wave Basis Set. *Comput. Mater. Sci.* **1996**, *6* (1), 15−50.
(53) Kresse, G.; Furthmüller, J. Efficient Iterative Schemes for *Ab Initio* Total-Energy Calculations Using a Plane-Wave Basis Set. *Phys. Rev. B* **1996**, *54* (16), 11169−11186.
(54) Wisesa, P.; McGill, K. A.; Mueller, T. Efficient Generation of Generalized Monkhorst-Pack Grids through the Use of Informatics. *Phys. Rev. B* **2016**, *93* (15), 155109.
(55) Hanwell, M. D.; Curtis, D. E.; Lonie, D. C.; Vandermeersch, T.; Zurek, E.; Hutchison, G. R. Avogadro: An Advanced Semantic Chemical Editor, Visualization, and Analysis Platform. *J. Cheminform* **2012**, *4* (1), 17.
(56) Kokalj, A. XCrySDen—a New Program for Displaying Crystalline Structures and Electron Densities. *J. Mol. Graph. Model.* **1999**, *17* (3−4), 176−179.
(57) Thimes, R. L.; Santos, A. V. B.; Chen, R.; Kaur, G.; Jensen, L.; Jenkins, D. M.; Camden, J. P. Using Surface-Enhanced Raman Spectroscopy to Unravel the Wingtip-Dependent Orientation of N-Heterocyclic Carbenes on Gold Nanoparticles. *J. Phys. Chem. Lett.* **2023**, *14* (18), 4219−4224.
(58) Navarro, J. J.; Das, M.; Tosoni, S.; Landwehr, F.; Bruce, J. P.; Heyde, M.; Pacchioni, G.; Glorius, F.; Roldan Cuenya, B. Covalent Adsorption of N-Heterocyclic Carbenes on a Copper Oxide Surface. *J. Am. Chem. Soc.* **2022**, *144* (36), 16267−16271.
(59) Franz, M.; Chandola, S.; Koy, M.; Zielinski, R.; Aldahhak, H.; Das, M.; Freitag, M.; Gerstmann, U.; Liebig, D.; Hoffmann, A. K.; Rosin, M.; Schmidt, W. G.; Hogan, C.; Glorius, F.; Esser, N.; Dähne, M. Controlled Growth of Ordered Monolayers of N-Heterocyclic Carbenes on Silicon. *Nat. Chem.* **2021**, *13* (9), 828−835.
(60) Lara, P.; Rivada-Wheelaghan, O.; Conejero, S.; Poteau, R.; Philippot, K.; Chaudret, B. Ruthenium Nanoparticles Stabilized by N-Heterocyclic Carbenes: Ligand Location and Influence on Reactivity. *Angew. Chem., Int. Ed.* **2011**, *50* (50), 12080−12084.
(61) Liske, A.; Verlinden, K.; Buhl, H.; Schaper, K.; Ganter, C. Determining the π-Acceptor Properties of N-Heterocyclic Carbenes by Measuring the ^{77} Se NMR Chemical Shifts of Their Selenium Adducts. *Organometallics* **2013**, *32* (19), 5269−5272.
(62) Huynh, H. V. Electronic Properties of N-Heterocyclic Carbenes and Their Experimental Determination. *Chem. Rev.* **2018**, *118* (19), 9457−9492.

https://doi.org/10.1021/acsomega.3c05376
ACS Omega 2023, 8, 37402−37412